

Analytical modelling and power density optimisation of a single phase dual active bridge for aircraft application

Niklas Fritz¹ ✉, Mohamed Rashed¹, Serhiy Bozhko¹, Fabrizio Cuomo², Pat Wheeler¹

¹The Department of Electrical and Electronic Engineering, The University of Nottingham, UK

²Leonardo Aircraft Division, Naples, Italy

✉ E-mail: niklas.fritz@rwth-aachen.de

eISSN 2051-3305

Received on 21st June 2018

Accepted on 1st August 2018

E-First on 21st May 2019

doi: 10.1049/joe.2018.8068

www.ietdl.org

Abstract: A design procedure for the dual active bridge (DAB) converter is presented, which aims to optimised power density and computational effort. When designing a DAB, the selection of circuit design parameters such as switching frequency, leakage inductance and semiconductor technologies is a complex question when targeting losses and weight minimisation of the final design. In this study, analytical models of the operating waveforms, the losses and the weight of all DAB components are developed. The proposed design algorithm is used for designing a 3 kW high-frequency DAB for an aircraft DC power system.

1 Introduction

The concept of the more electric aircraft promotes the use of electrical instead of traditional hydraulic, pneumatic or mechanical systems [1, 2]. The advantages are reduced cost, reduced fuel consumption, lower weight and less environmental impact. This results in an increase in the power rating of the aircraft power system and imposes the use of high-voltage DC buses. Hence, DC/DC converters will play an important role in the management of electrical power in future aircraft. The ASPIRE project, part of the Clean Sky 2 Joint Undertaking, aims to design an electrical power system for next-generation aircraft. One goal of the ASPIRE project is to design an ultra-light and efficient isolated bidirectional DC/DC converter, interfacing the 28 V and 270 V DC buses at 3 kW rated power. The dual active bridge (DAB) is a suitable topology [3] for such application.

The design of the DAB implies the choice of many converter parameters such as switching frequency, leakage and magnetising inductances, semiconductor devices and magnetic materials in order to minimise the total losses and weight of the converter. Such large numbers of design parameters make the design of the DAB a tedious and complex process.

Existing analytical modelling-based design approaches rarely consider modelling of power losses or weight of converter components [4–8]. Moreover, many DAB designs are very specific to the target application [9–11].

In this paper, an efficient design procedure based on analytical modelling of the DAB is proposed and applied to optimise the converter for the highest power density with minimal computational effort. The proposed optimisation technique, visualised in Fig. 1, consists of three steps. It starts with the calculation of the current and voltage waveforms and other electrical variables of the DAB, e.g. the RMS current. In the second step, these variables are used to assess converter losses. The third layer of the optimisation technique is an analytical model of the component weights used to assess the power density.

The paper is organised in six sections. Section 2 gives an overview of the DAB. Section 3 introduces the analytical model of the DAB operating waveforms. In Sections 4 and 5, loss and weight analytical models are given. Finally, Section 6 gives an example design of the DAB for the ASPIRE project.

2 Single phase dual active bridge

The DAB was first proposed in [3] and its generic single phase variant is depicted in Fig. 2.

The single phase DAB consists of two active H-bridges and a high frequency transformer. V_P and V_S denote the primary and secondary side DC voltages, respectively. The original modulation strategy is called single phase shift (SPS) modulation, which is depicted in Fig. 3 [3]. Both H-bridges operate at 50% duty cycle, but phase shifted in time by the angle ϕ . The output voltages of the

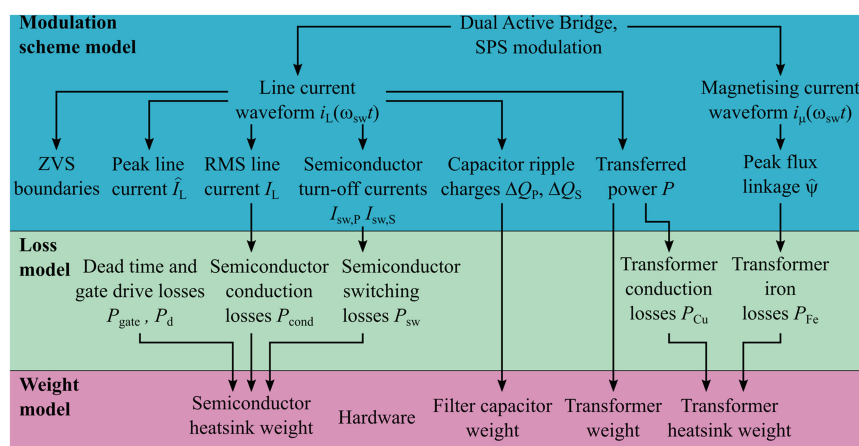


Fig. 1 Flowchart of the proposed design algorithm

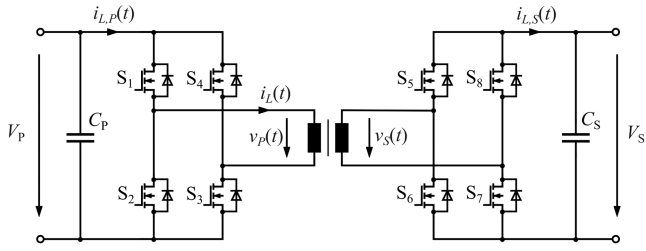


Fig. 2 Dual active bridge topology, single phase

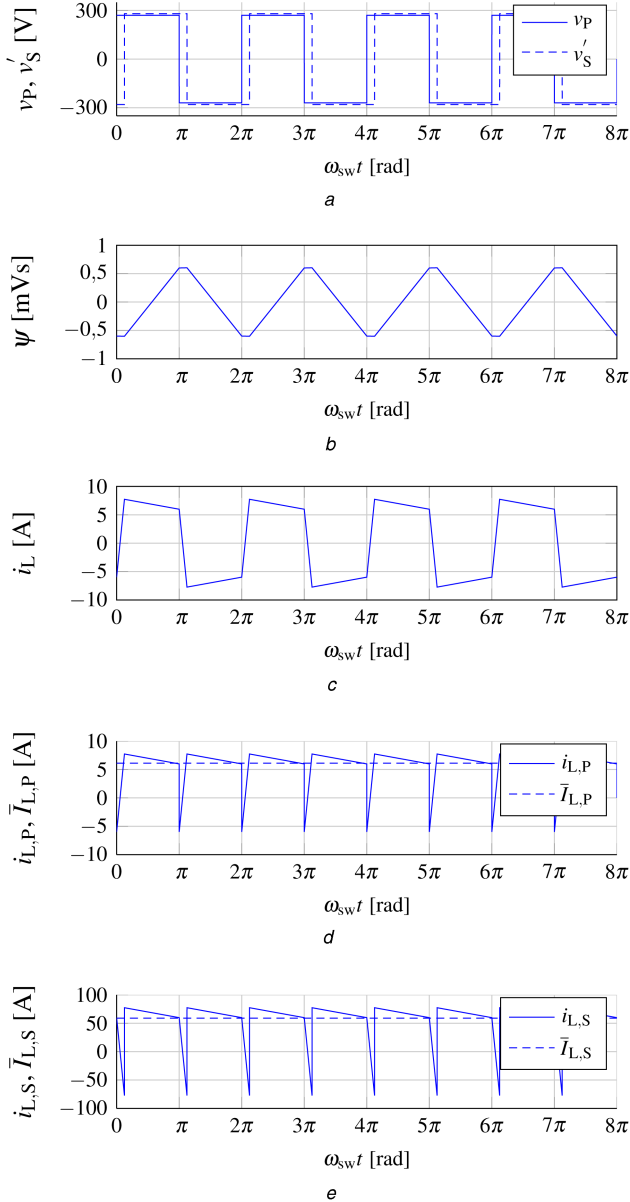


Fig. 3 Generic single phase shift (SPS) modulation

(a) Output voltages of the H-bridges, (b) Transformer flux linkage, (c) AC link current, (d) Primary side rectified current and primary side DC current, (e) Secondary side rectified current and secondary side DC current

primary and secondary side H-Bridge are denoted $v_P(t)$ and $v_S(t)$, respectively. Using the transformer turns ratio n , all secondary side quantities are referred to the primary side and indicated by a dash. The waveforms $v_P(t)$ and $v'_S(t)$ are shown in Fig. 3a. The voltage difference $v_P(t) - v'_S(t)$ drops across the leakage inductance L of the transformer and results in a quasi-square wave AC current in the transformer, $i_L(t)$ (see Fig. 3c). As shown in Fig. 2, the input currents of the primary and secondary side H-bridge are denoted by $i_{L,P}(t)$ and $i'_{L,S}(t)$, respectively. They are plotted in Figs. 3d and e, respectively. The current ripples are filtered by the DC-link

capacitors C_P and C_S . The average currents provided by the primary and secondary side DC buses are denoted by $\bar{i}_{L,P}$ and $\bar{i}'_{L,S}$, respectively. The transferred power P is given in (1), where ϕ denotes the phase shift angle between $v_P(t)$ and $v'_S(t)$ and f_{sw} denotes the switching frequency [3]

$$P = \frac{V_P V'_S}{2\pi^2 f_{sw} L} \cdot \phi(\pi - |\phi|) \quad (1)$$

Maximum power is transferred for a phase shift angle of $\pi/2$. The turn-off transition of the devices in both H-Bridges is generally hard-switched, whereas for the turn-on transition, zero voltage switching (ZVS) is achieved for most operating points.

3 Analytical model of SPS modulation

Before analysing the losses and the weight of the DAB, the analytical model of SPS modulation is derived from two current waveforms, namely the current $i_L(\omega_{sw}t)$ in the AC link and the magnetising current $i_M(\omega_{sw}t)$. Due to waveform symmetries (see Fig. 3), it is sufficient to regard half a switching period. The following conventions are made, which are visualised in Fig. 4: For positive phase shifts $\phi \geq 0$, the rising edge of the primary voltage $v_P(t)$ is located at $\omega_{sw}t = 0$ and the rising edge of the secondary voltage $v'_S(t)$ is delayed to $\omega_{sw}t = \phi$. For negative phase shifts $\phi < 0$, the rising edge of the secondary voltage is located at $\omega_{sw}t = 0$ and the rising edge of the primary voltage is delayed to $\omega_{sw}t = |\phi|$.

3.1 Line current and derived quantities

The current waveform $i_L(\omega_{sw}t)$ is obtained by integrating the output voltage difference of the H-bridges, $v_P(t) - v'_S(t)$. For keeping the model simple, ohmic resistances and the magnetising inductance L_m are neglected. The resulting current waveform as well as its initial values at $\omega_{sw}t = 0$ and $\omega_{sw}t = |\phi|$ are given as follows:

$$i_L(\omega_{sw}t) = \begin{cases} i_L(0) + \text{sgn}(\phi) \frac{V_P + V'_S}{\omega_{sw}L} \omega_{sw}t & \text{for } 0 \leq \omega_{sw}t < |\phi| \\ i_L(|\phi|) + \frac{V_P - V'_S}{\omega_{sw}L} (\omega_{sw}t - |\phi|) & \text{for } |\phi| \leq \omega_{sw}t < \pi \end{cases} \quad (2)$$

$$i_L(0) = -\frac{1}{2} \left(\frac{V_P + V'_S}{\omega_{sw}L} \phi + \frac{V_P - V'_S}{\omega_{sw}L} (\pi - |\phi|) \right) \quad (3)$$

$$i_L(|\phi|) = +\frac{1}{2} \left(\frac{V_P + V'_S}{\omega_{sw}L} \phi - \frac{V_P - V'_S}{\omega_{sw}L} (\pi - |\phi|) \right) \quad (4)$$

Depending on the sign of the phase shift angle ϕ , the two H-bridges either switch at the time instant $\omega_{sw}t = 0$ or $\omega_{sw}t = |\phi|$. For example, for $\phi \geq 0$, the primary H-bridge switches at $\omega_{sw}t = 0$ and for $\phi < 0$, it switches at $\omega_{sw}t = |\phi|$. Therefore, it is important to calculate the current which has to be switched off by the H-bridges, regardless of the respective time instant. For the primary and the secondary H-bridges, the turn-off currents are given in (5) and (6), respectively.

$$I_{sw,P} = -\frac{1}{2} \left(\frac{V_P + V'_S}{\omega_{sw}L} |\phi| + \frac{V_P - V'_S}{\omega_{sw}L} (\pi - |\phi|) \right) \quad (5)$$

$$I'_{sw,S} = +\frac{1}{2} \left(\frac{V_P + V'_S}{\omega_{sw}L} |\phi| - \frac{V_P - V'_S}{\omega_{sw}L} (\pi - |\phi|) \right) \quad (6)$$

From (5) and (6), the conditions for ZVS of the primary and secondary side H-bridge, respectively, are derived. At the

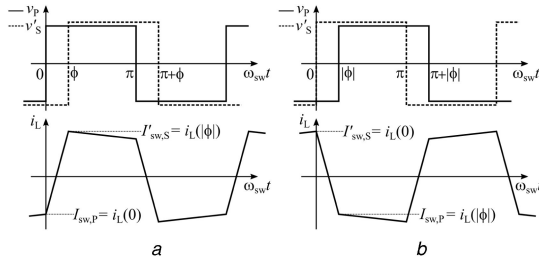


Fig. 4 Timing conventions for the analytical models for (a) $\phi \geq 0$ and (b) $\phi < 0$

switching instant, the current has to flow in the antiparallel diodes of the switches to achieve ZVS. This is formulated as follows:

$$I_{sw,P} < 0 \Rightarrow V_P > V'_S \left(1 - 2\frac{|\phi|}{\pi}\right) \quad (7)$$

$$I'_{sw,S} > 0 \Rightarrow V'_S > V_P \left(1 - 2\frac{|\phi|}{\pi}\right) \quad (8)$$

As $|\phi| \leq \pi/2$, the second term in (7) and (8) is always positive. It is clear that if the ratio of the DC voltages does not match the transformer turns ratio n , i.e. $V_P \neq V'_S$, the ZVS conditions will be violated at low load [12].

The peak value of the AC link current i_L is denoted by \hat{I}_L

$$\begin{aligned} \hat{I}_L &= \max[|i_L(0)|, |i_L(|\phi|)] \\ &= \frac{|V_P - V'_S|}{2\omega_{sw}L} \pi + \frac{(V_P + V'_S) - |V_P - V'_S|}{2\omega_{sw}L} |\phi| \end{aligned} \quad (9)$$

By squaring (2) and integrating, the RMS value of the AC link current, I_L , is also derived

$$I_L = \frac{1}{\omega_{sw}L} \sqrt{\frac{\pi^2}{12}(V_P - V'_S)^2 + V_P V'_S \left(\phi^2 - \frac{8}{12\pi} |\phi|^3\right)} \quad (10)$$

The input currents of the two H-bridges, $i_{L,P}(t)$ and $i'_{L,S}(t)$, as shown in Figs. 3d and e, are obtained by changing the sign of i_L in a way such that it accounts for the switching state of the respective H-bridges. From the waveforms, the average DC currents $\bar{I}_{L,P}$ and $\bar{I}'_{L,S}$ are obtained by averaging

$$\bar{I}_{L,P} = \frac{V'_S}{\pi\omega_{sw}L} \phi(\pi - |\phi|) \quad (11)$$

$$\bar{I}'_{L,S} = \frac{V_P}{\pi\omega_{sw}L} \phi(\pi - |\phi|) \quad (12)$$

Multiplying the currents (11) and (12) with the respective DC voltage yields the power transfer equation (1). If pure DC currents are assumed at the two ports of the DAB, the current ripples of $i_{L,P}(t)$ and $i'_{L,S}(t)$ are assumed to flow into the DC-link capacitors C_P and C_S . The ripple charges ΔQ_P and $\Delta Q'_S$ are derived from the areas enclosed by the waveforms $(i_{L,P}(\omega_{sw}t) - \bar{I}_{L,P})$ and $(i'_{L,S}(\omega_{sw}t) - \bar{I}'_{L,S})$. The results are shown in

(see (13))

(see (14))

The required DC-link capacitor sizes are calculated by dividing the ripple charges given in (13) and (14) by the permissible voltage ripples ΔV_P and $\Delta V'_S$. The energies needed to be stored in the capacitors C_P and C_S are given by E_{CP} and E_{CS} in (15) and (16), respectively.

$$E_{CP} = \frac{1}{2} C_P (V_P + \Delta V_P)^2 = \frac{V_P^2 \Delta Q_P}{2\Delta V_P} + V_P \Delta Q_P + \frac{\Delta V_P \Delta Q_P}{2} \quad (15)$$

$$\begin{aligned} E_{CS} &= \frac{1}{2} C_S (V'_S + \Delta V'_S)^2 \\ &= n \left(\frac{V_S^2 \Delta Q'_S}{2\Delta V'_S} + V'_S \Delta Q'_S + \frac{\Delta V'_S \Delta Q'_S}{2} \right) \end{aligned} \quad (16)$$

3.2 Magnetising current and derived quantities

The transformer is modelled by its T-equivalent circuit, which is shown in Fig. 5. The inductances $L_{P\sigma}$ and $L'_{S\sigma}$ describe the leakage inductances of the transformer on both the primary and secondary windings, so that $L = L_{P\sigma} + L'_{S\sigma}$. The ratio of leakage inductances r , the ratio of voltages d and the transformer utilisation factor λ are defined as follows

$$r = \frac{L_{P\sigma}}{L'_{S\sigma}} \quad (17)$$

$$d = \frac{V_P}{V'_S} \quad (18)$$

$$\lambda = 1 - \frac{|V_P - rV'_S|}{V_P + rV'_S} = 1 - \frac{|d - r|}{d + r} \quad (19)$$

Using definitions (17)–(19) and the assumption that the leakage inductances are much smaller than L_m , the virtual voltage v_m on the

$$\Delta Q_P = \begin{cases} \frac{(2V'_S\phi^2 + \pi^2(V_P - V'_S)^2)}{8\omega_{sw}^2 L \pi^2 (V_P - V'_S)} & \text{for } V_P > V'_S \text{ and } |I'_{sw,S}| < |\bar{I}_{L,P}| \\ \frac{(2V'_S|\phi|(2\pi - |\phi|) + \pi^2(V_P - V'_S)^2)}{8\omega_{sw}^2 L \pi^2 (V_P + V'_S)} & \text{for } \begin{cases} V_P = V'_S \text{ or} \\ V_P > V'_S \text{ and } |I'_{sw,S}| \geq |\bar{I}_{L,P}| \text{ or} \\ V_P < V'_S \text{ and } |I_{sw,P}| \geq |\bar{I}_{L,P}| \end{cases} \\ \frac{V'_S(2V'_S\phi^2 - (\pi^2 - 2\pi|\phi|)(V_P - V'_S)^2)}{4\omega_{sw}^2 L \pi^2 (V'_S - V_P)} & \text{for } V_P < V'_S \text{ and } |I_{sw,P}| < |\bar{I}_{L,P}| \end{cases} \quad (13)$$

$$\Delta Q'_S = \begin{cases} \frac{V_P(2V_P\phi^2 + (\pi^2 - 2\pi|\phi|)(V_P - V'_S)^2)}{4\omega_{sw}^2 L \pi^2 (V_P - V'_S)} & \text{for } V_P > V'_S \text{ and } |I'_{sw,S}| < |\bar{I}'_{L,S}| \\ \frac{(2V_P|\phi|(2\pi - |\phi|) - \pi^2(V_P - V'_S)^2)}{8\omega_{sw}^2 L \pi^2 (V_P + V'_S)} & \text{for } \begin{cases} V_P = V'_S \text{ or} \\ V_P > V'_S \text{ and } |I'_{sw,S}| \geq |\bar{I}'_{L,S}| \text{ or} \\ V_P < V'_S \text{ and } |I_{sw,P}| \geq |\bar{I}'_{L,S}| \end{cases} \\ \frac{(2V_P\phi^2 - \pi^2(V_P - V'_S)^2)}{8\omega_{sw}^2 L \pi^2 (V'_S - V_P)} & \text{for } V_P < V'_S \text{ and } |I_{sw,P}| < |\bar{I}'_{L,S}| \end{cases} \quad (14)$$

magnetising inductance can be calculated from the circuit in Fig. 5 as in (20)

$$v_m(t) = \frac{v_p(t) + r v_s'(t)}{1 + r} = \begin{cases} v_p(t) & \text{for } r = 0 \\ \frac{v_p(t) + v_s'(t)}{2} & \text{for } r = 1 \\ v_s'(t) & \text{for } r \rightarrow \infty \end{cases} \quad (20)$$

By integrating the voltage of (20), the magnetising current waveform $i_\mu(\omega_{sw}t)$ is obtained

$$i_\mu(\omega_{sw}t) = \begin{cases} i_\mu(0) + \frac{\text{sgn}(\phi) (V_p - r V_s')}{(1 + r) \omega_{sw} L_m} \omega_{sw} t & \text{for } 0 \leq \omega_{sw} t < |\phi| \\ i_\mu(|\phi|) + \frac{V_p + r V_s'}{(1 + r) \omega_{sw} L_m} (\omega_{sw} t - |\phi|) & \text{for } |\phi| \leq \omega_{sw} t < \pi \end{cases} \quad (21)$$

$$i_\mu(0) = -\frac{1}{2} \left(\frac{V_p - r V_s'}{(1 + r) \omega_{sw} L_m} \phi + \frac{V_p + r V_s'}{(1 + r) \omega_{sw} L_m} (\pi - |\phi|) \right) \quad (22)$$

$$i_\mu(|\phi|) = +\frac{1}{2} \left(\frac{V_p - r V_s'}{(1 + r) \omega_{sw} L_m} \phi - \frac{V_p + r V_s'}{(1 + r) \omega_{sw} L_m} (\pi - |\phi|) \right) \quad (23)$$

The flux linkage in the transformer core is given by $\psi = L_m i_\mu$ (see Fig. 3b). In analogy to (9), the peak magnetising current \hat{I}_μ and the peak flux linkage $\hat{\psi}$ are calculated as

$$\hat{I}_\mu = \max [|i_\mu(0)|, |i_\mu(|\phi|)|] = \frac{V_p + r V_s'}{2(1 + r) \omega_{sw} L_m} \pi - \frac{(V_p + r V_s') - |V_p - r V_s'|}{2(1 + r) \omega_{sw} L_m} |\phi| \quad (24)$$

$$\hat{\psi} = \frac{V_p + r V_s'}{2(1 + r) \omega_{sw}} \pi - \frac{(V_p + r V_s') - |V_p - r V_s'|}{2(1 + r) \omega_{sw}} |\phi| \quad (25)$$

From (25), it becomes clear that the maximum peak flux linkage in the transformer core, $\hat{\psi}_{\max}$, is given as follows:

$$\hat{\psi}_{\max} = \frac{V_p + r V_s'}{2(1 + r) \omega_{sw}} \pi \quad (26)$$

The flux density B cannot be calculated as the number of turns and the core area are still unknown. However, if a reasonable value is assumed for the maximum flux density \hat{B}_{\max} , the per-unit utilisation of the transformer can be derived as given by (27), based on the utilisation factor λ defined in (19).

$$\frac{\hat{B}}{\hat{B}_{\max}} = \frac{\hat{\psi}}{\hat{\psi}_{\max}} = 1 - \lambda \frac{|\phi|}{\pi} \quad (27)$$

4 Analytical loss model

A loss model is required to evaluate efficiency and the cooling effort. For the DAB under design, MOSFETs are used. The conduction losses are calculated using the on-state resistances $R_{DS,P}$ and $R_{DS,S}$ of the MOSFETs in the primary and secondary side H-bridges, respectively. The AC link current always flows through two switches of each H-bridge simultaneously. Also the transformer contributes to conduction losses with its total equivalent copper resistance R_{Cu} . High-frequency loss components due to skin and proximity effects are neglected for simplicity. Therefore, the total conduction losses of the converter, $P_{\text{cond,tot}}$, are expressed as a function of a total equivalent resistance R_{tot}

$$R_{\text{tot}} = 2R_{DS,P} + 2n^2 R_{DS,S} + R_{Cu} \quad (28)$$

$$P_{\text{cond,tot}} = R_{\text{tot}} \cdot I_L^2 \quad (29)$$

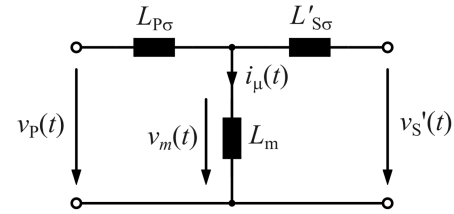


Fig. 5 T-equivalent circuit of the transformer

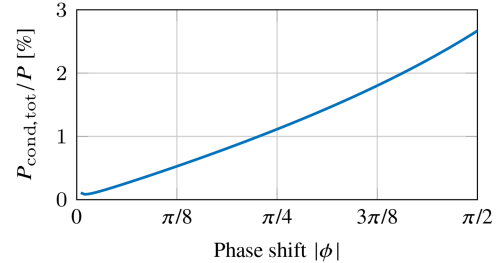


Fig. 6 Share of conduction losses in transferred power. $V_p = 270$ V, $V_s = 28$ V, $n = 10$, $f_{sw} = 100$ kHz, $L = 25$ μ H, $R_{\text{tot}} = 0.2$ Ω

The share of conduction losses with respect to the total transferred power, $P_{\text{cond,tot}}/P$, can be calculated using (10) in (29) as well as (1). It is plotted as a function of the phase shift angle in Fig. 6. The maximum phase shift should be limited to a value below the theoretical limit of $\pi/2$, to enhance efficiency.

Furthermore, the overall power which is required to drive the power MOSFETs is calculated using their gate charges $Q_{g,P}$ and $Q_{g,S}$ and the gate voltages $V_{g,P}$ and $V_{g,S}$:

$$P_{\text{gate}} = 4f_{sw} Q_{g,P} V_{g,P} + 4f_{sw} Q_{g,S} V_{g,S} \quad (30)$$

During the dead time periods $t_{d,P}$ and $t_{d,S}$, the body diodes of the power MOSFETs conduct, causing additional losses due to the forward voltage drop $V_{SD,P}$ and $V_{SD,S}$

$$P_d = 4f_{sw} \cdot (t_{d,P} V_{SD,P} |I_{sw,P}| + t_{d,S} V_{SD,S} |n I'_{sw,S}|) \quad (31)$$

The switching losses of the MOSFETs are hard to describe analytically and as the DAB operates under ZVS, only the turnoff losses have to be considered. For estimating the switching losses, it is possible to use the following approaches, which are sorted in decreasing order of accuracy and in increasing order of ease of implementation:

- Experimental data
- Device models by the manufacturers
- Switching loss data from the datasheets
- Analytical estimates, e.g. as shown in [13]

Finally, the iron losses of the transformer are calculated using the improved generalised Steinmetz equation (iGSE):

$$P_{Fe} = Vol_{Fe} f_{sw} \int_0^{f_{sw}^{-1}} k_i \left| \frac{dB}{dt} \right|^\alpha \Delta \hat{B}_{pp}^{\beta-\alpha} dt, \quad (32)$$

where

$$k_i = \frac{k}{(2\pi)^{\alpha-1} \int_0^{2\pi} |\cos \theta|^\alpha \cdot 2^{\beta-\alpha} d\theta} \quad (33)$$

k , α and β are material specific data, Vol_{Fe} is the iron volume and $\Delta \hat{B}_{pp}$ is the peak-to-peak core flux density. The cross-sectional area of the core and the number of turns are unknown design information. Therefore, the per-unit quantity \hat{B}/\hat{B}_{\max} from (27) is used in (32), which now can be solved analytically:

$$P_{Fe} = 2^{\alpha+\beta} Vol_{Fe} k_i f_{sw}^{\alpha} \hat{B}_{max}^{\beta} \left(1 - \lambda \frac{|\phi|}{\pi}\right)^{\beta-\alpha} \left(1 - \lambda_{\alpha} \frac{|\phi|}{\pi}\right) \quad (34)$$

where $\lambda_{\alpha} = 1 - \left(\frac{d-r}{d+r}\right)^{\alpha}$

The transformer core volume can be calculated using the stored energy E_m . It is expressed by the peak flux linkage and the magnetising current on the one hand and by the peak flux density on the other hand

$$E_m = \frac{1}{2} L_m \hat{I}_{\mu}^2 = \frac{1}{2} \hat{\psi}_{max} \hat{I}_{\mu} = Vol_{Fe} \cdot \frac{\hat{B}_{max}^2}{2\mu_0\mu_r} \quad (35)$$

$$\Rightarrow Vol_{Fe} = \frac{\mu_0\mu_r \hat{\psi}_{max}^2 \hat{I}_{\mu}}{\hat{B}_{max}^2}$$

5 Analytical weight model

In this section, all components of the DAB as well as the losses are mapped to weights. Losses affect the weight in terms of the size of the heat sink. Its thermal resistance is denoted $R_{th,HS}$. Research [14] proposes a figure of merit, which is a material constant, to estimate the weight of a heat sink m_{HS}

$$FOM_{HS} = \frac{1}{m_{HS} \cdot R_{th,HS}} \quad (36)$$

Knowing the losses from the model in Section 4 and the maximum permissible temperatures, (36) can be used to translate the required thermal resistance of the cooling system into its weight.

The weight of the input and output capacitors is proportional to the stored energy which has been derived in (15) and (16). To evaluate the weight, energy densities of suitable capacitor technologies may be researched.

The literature [15] states that the weight of the transformer m_{Tr} is proportional to the area product A_p , i.e. the product of core area A_c and winding window area A_w , by a factor K_W

$$m_{Tr} = K_W \cdot A_p^{3/4} \quad (37)$$

Describing the window area in terms of the copper fill factor k_u , the number of turns N , the peak current density \hat{J}_{max} and the maximum AC link RMS current $I_{L,max}$, and describing the core area in terms of maximum flux linkage $\hat{\psi}_{max}$ and maximum flux density \hat{B}_{max} , the area product is found

$$A_p = A_c \cdot A_w = \frac{\hat{\psi}_{max}}{N \hat{B}_{max}} \cdot \frac{2NI_{L,max}}{k_u \hat{J}_{max}} = \frac{2P_{max}}{4f_{sw} k_u \hat{B}_{max} \hat{J}_{max}} \quad (38)$$

An alternative to this approach is to research existing transformers and find empirical relationships of weight and power.

6 Optimisation example

Combining the equations from the previous sections connects basic design parameters to the weights of the DAB components and enables optimisation of power density. As an example, a preliminary design of the DAB of the ASPIRE project is presented in this section. Table 1 lists the converter parameters. The analysis is performed for a wide range of switching frequencies and different MOSFETs, including modern SiC and GaN devices. For minimisation of the conduction losses, the maximum phase shift is reduced below the theoretical limit of $\pi/2$. This decides the leakage inductance according to (1).

For estimating the switching losses, the equations from [13] are used. Moreover, the thermal figure of merit for an aluminum cooling system including fan is needed. From the results of [16, 17], a value of $FOM_{HS} = 15 \text{ W/(kgK)}$ is a reasonable choice. Additionally, for the filter capacitors C_p and C_s , a research of

Table 1 Parameters of the ASPIRE converter design

DC voltages	$V_P; V_S$	270 V; 28 V
rated power	P	3 kW
ambient temperature	T_{amb}	70°C
switching frequency	f_{sw}	50–1000 kHz
transformer turns ratio	n	10
max. SPS phase shift angle	$ \phi _{max}$	45°
max. magnetising current	\hat{I}_{μ}	1 A
max. junction temperature	$T_{j,max}$	125°C
max. transformer temperature	$T_{Tr,max}$	125°C
permissible ripple voltages	$\Delta V_P; \Delta V_S$	4 V; 1 V
magnetic material	Ferroxcube	3C96
maximum flux density	B_{max}	0.5 B_{sat}
primary side MOSFETs	Infineon	IPT65R033G7 (Si)
	Wolfspeed	C3M0065090J (SiC)
	GaN systems	GS66516T (GaN)
secondary side MOSFETs	Infineon	IPT012N08N5 (Si)
	EPC	4x EPC2021 (GaN)

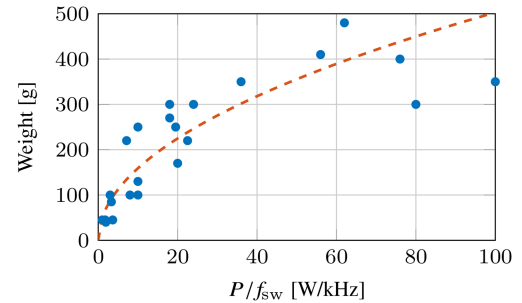


Fig. 7 Weight data of existing planar transformers and empirical model

ceramic capacitors with suitable voltage ratings gave power densities of 41 J/kg and 19 J/kg, respectively. For the transformer, an efficiency of 99% is assumed, yielding a copper resistance of $R_{Cu} = 0.2 \Omega$. A ratio of $r = 1$ for the leakage inductances is assumed. Planar transformers with similar power ratings from different companies have been researched and the following empirical weight model has been fitted to the collected data:

$$m_{Tr} \approx 1.59 \frac{\text{kg}}{\sqrt{\text{W/Hz}}} \cdot \sqrt{\frac{P}{f_{sw}}} \quad (39)$$

The researched transformers weights as well as the empirical model from (39) are shown in Fig. 7. The magnetic material parameters k , α and β are obtained from the loss density graphs from the datasheet. Moreover, a net weight of 140 g for the printed circuit board (PCB), the hardware, the semiconductors and additional circuitry as gate drivers and sensors is assumed.

In Fig. 8, the theoretical power density for this example design is shown. The proposed target design is indicated by the dot. It reaches a power density of 6 kW/kg at $f_{sw} = 250 \text{ kHz}$. Finally, Fig. 9 shows the weight and the loss breakdown of the design which is indicated by the dot in Fig. 8. Generating these results in MATLAB requires few seconds of computation time.

7 Conclusion

In this paper, analytical models of the operating waveforms, the losses and the component weights of a single phase DAB are developed and used in a design optimisation algorithm. The design approach is easy to implement and is computationally efficient. The developed design optimisation algorithm is a useful tool for the designer to obtain initial and fast designs of DAB and to identify the impact of specific design decisions on the power density of the DAB.

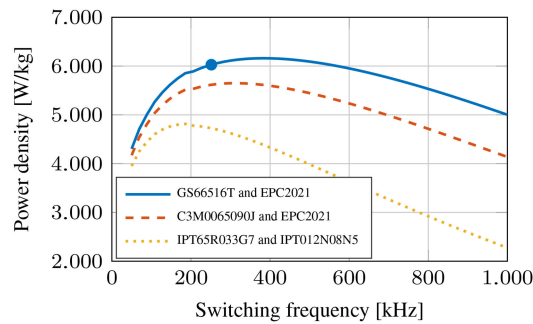


Fig. 8 Power density as a function of switching frequency for different semiconductor device combinations

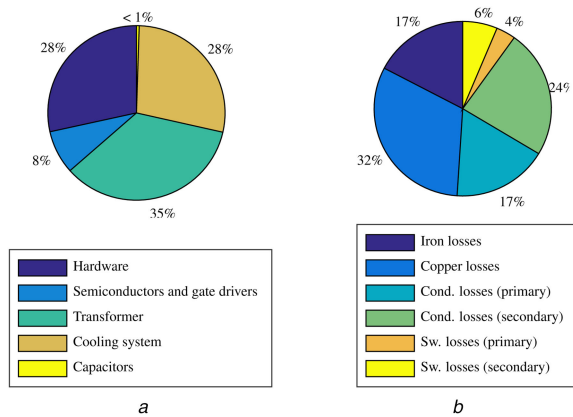


Fig. 9 Weight and loss breakdown

(a) Weight breakdown of the example design (total weight: 500 g), (b) Loss breakdown at $P = 3$ kW of the example design (total losses: 111 W)

8 Acknowledgment

This project has received funding from the Clean Sky 2 Joint Undertaking under the European Union's Horizon 2020 research and innovation programme under grant agreement No 717091.

9 References

[1] Wheeler, P., Bozhko, S.: 'The more electric aircraft: technology and challenges', *IEEE Electrific. Mag.*, 2014, **2**, (4), pp. 6–12

[2] Wheeler, P.: 'Technology for the more and all electric aircraft of the future'. 2016 IEEE Int. Conf. on Automatica (ICA-ACCA), Curico, Chile, 2016

[3] De Doncker, R. W., Divan, D. M., Kheraluwala, M.H., *et al.*: 'A three-phase soft-switched high-power-density dc/dc converter for high-power applications', *IEEE Trans. Ind. Appl.*, 1991, **27**, (1), pp. 63–73

[4] Fontana, C., Forato, M., Bertoluzzo, M., *et al.*: 'Design characteristics of SAB and DAB converters'. Intl. Conf. on Optimization of Electrical & Electronic Equipment (OPTIM), Side, Turkey, 2015

[5] van Hoek, H., Jacobs, K., Neubert, M., *et al.*: 'Performance analysis of an analytical calculation tool for dual-active-bridge converters'. IEEE Int. Conf. on Power Electronics and Drive Systems, Sydney, Australia, 2015

[6] Rodriguez, A., Vazquez, A., Lamar, G., *et al.*: 'Different purpose design strategies and techniques to improve the performance of a dual active bridge with phase-shift control', *IEEE Trans. Power Electron.*, 2015, **30**, (2), pp. 790–804

[7] Choi, H., Park, H., Jung, J., *et al.*: 'Design methodology of dual active bridge converter for solid state transformer application in smart grid'. Int. Conf. on Power Electronics and ECCE Asia (ICPE-ECCE Asia), Seoul, South Korea, 2015

[8] Zhao, B., Song, Q., Liu, W., *et al.*: 'A synthetic discrete design methodology of high-frequency isolated bidirectional DC/DC converter for grid-connected battery energy storage system using advanced components', *IEEE Trans. Ind. Electron.*, 2014, **61**, (10), pp. 5402–5410

[9] Krismer, F., Kolar, J. W.: 'Efficiency-optimised high-current dual active bridge converter for automotive applications', *IEEE Trans. Ind. Electron.*, 2012, **59**, (7), pp. 2745–2760

[10] Gammeter, C., Krismer, F., Kolar, J. W., *et al.*: 'Comprehensive conceptualization, design, and experimental verification of a weight-optimized all-SiC 2 kV/700 V DAB for an airborne wind turbine', *IEEE J. Emerging Sel. Topics Power Electron.*, 2016, **4**, (2), pp. 638–656

[11] Joebges, P., Hu, J., De Doncker, R. W., *et al.*: 'Design method and efficiency analysis of a DAB converter for PV integration in DC grids'. IEEE Southern Power Electronics Conf. (SPEC), Auckland, New Zealand, Dec. 2016

[12] Taraborrelli, S., Spenke, R., De Doncker, R. W., *et al.*: 'Bidirectional dual active bridge converter using a tap changer for extended voltage ranges'. 2016 18th European Conf. on Power Electronics and Applications (EPE '16 ECCE Europe), Institute of Electrical and Electronics Engineers (IEEE), Karlsruhe, Germany, Sept. 2016

[13] Vishay Intertechnology, Inc.: 'Device application note AN608A – power MOSFET basics: understanding gate charge and using it to assess switching performance', 2016. Available at: <http://www.vishay.com/doc?73217>

[14] Icoz, T., Arik, M.: 'Lightweight high performance thermal management with advanced heat sinks and extended surfaces', *IEEE Trans. Compon. Packag. Technol.*, 2010, **33**, (1), pp. 161–166

[15] McLyman, W. T.: 'Transformer and inductor design handbook' (Marcel Dekker, Inc., New York, 2004)

[16] Gammeter, C., Krismer, F., Kolar, J. W., *et al.*: 'Weight optimization of a cooling system composed of fan and extruded-fin heat sink', *IEEE Trans. Ind. Appl.*, 2015, **51**, (1), pp. 509–520

[17] Ning, P., Lei, G., Wang, F., *et al.*: 'Selection of heat-sink and fan for high-temperature power modules under weight constraint'. Twenty-Third Annual IEEE Applied Power Electronics Conf. and Exposition, Austin, TX, USA, 2008